



Numerical simulation of failure in steel posttensioned connections under cyclic loading



Azin Al Kajbaf, Nader Fanaie*, Kaveh Faraji Najarkolaie

Department of Civil Engineering, K. N. Toosi University of Technology, Tehran, Iran

ARTICLE INFO

Keywords:

Posttensioned steel connection
failure mode
fracture modeling
strand yielding
low yield point steel

ABSTRACT

Posttensioned energy dissipation (PTED) connections are systems employed in structures to prevent the earthquake imposed failure and minimize the post-earthquake damage by eliminating residual deformation and dissipating seismic energy. Ever increasing trend in research regarding posttensioned frames has raised the necessity toward studying failure modes in these systems to identify and avoid the probable damages. This paper investigates the possibility of modeling the various failure modes in a relatively complex steel frame. Three PTED connections with bolted top-and-seat angles as energy dissipater devices with different failure modes including beam local buckling, strand yielding and angle fracture are simulated under cyclic loading. To remove the convergence difficulty in the analysis, explicit method has been used which is capable of modeling fracture and failure without convergence checking. Comparing the analytical results with experimental data indicates finite element models are able to predict the behavior of PTED connections. This research demonstrates that with existing methods for modeling failure of steel and cable which are mostly used in small scale, the failures modes of full scale complicated steel frames can be captured with sufficient precision. Furthermore, an investigation has been done to evaluate one of the applications of modeling failure which is finding a solution to enhance the behavior of a member which is subjected to damage. In this study a method has been presented to resolve fracture in energy dissipater devices. Low yield point (LYP) steel has been used in the angles which significantly improve the behavior of PTED connection by postponing the fracture point from 4% to 7% drift. It also results in up to 222% increase in total energy dissipation capacity of the connection.

1. Introduction

Following every major earthquake, particular seismic deficiencies are revealed in current structural systems which are required to be accurately determined and resolved in subsequent designs. The 1994 Northridge earthquake resulted in failure of more than one hundred steel moment resisting frames (MRFs).

Many factors were involved in developing damage; nevertheless the majority of fractures started from the field weld which connected the beam bottom flange to the column flange [1].

Post Northridge earthquake, several experimental and numerical studies were carried out in order to develop an improved MRF including, connections retrofitted with locally reduced beam section (RBS) [2], connection with cover plates [3], connections rehabilitated with RBS or welded haunches [4] and side plates [5]. Although these structures have better performance and can survive a design level earthquake, the damage to the structural elements such as yielding and buckling of the beams will cause the buildings

* Corresponding author.

E-mail addresses: aalkajbaf@mail.kntu.ac.ir (A. Al Kajbaf), fanaie@kntu.ac.ir (N. Fanaie), kfaraji@mail.kntu.ac.ir (K. Faraji Najarkolaie).

<https://doi.org/10.1016/j.engfailanal.2018.04.024>

Received 14 September 2017; Received in revised form 19 March 2018; Accepted 12 April 2018

Available online 14 April 2018

1350-6307/ © 2018 Elsevier Ltd. All rights reserved.

Nomenclature			
E, ν	Young's modulus & poisson's ratio	A_R	Reduction in area of a uniaxial axisymmetric tensile specimen
σ_y, σ_u	Yield & ultimate stress	ω_D	Damage index
$\sigma_{nom}, \epsilon_{nom}$	Nominal stress & strain	$\dot{\epsilon}_t^{pl}$	Plastic strain rate during the time increment
ϵ_{ln}^{pl}	Logarithmic plastic strain	\bar{u}^{pl}	Equivalent plastic displacement
σ_{true}	True stress	L	Characteristic length of the element
R, R_f	Void radius & void radius at fracture	M	Mass matrix
σ_m	Hydrostatic stress	F, R	Internal & external load vector
σ_e	Equivalent stress	j	Increment number
η, η_0	Stress triaxiality & triaxiality at uniaxial tension	ω_{max}	Maximum eigenvalue of the system
$\epsilon_e, \epsilon_e^{pl}$	Equivalent strain & equivalent plastic strain	ξ_{max}	Damping ratio corresponding to highest eigenvalue in the system
$\sigma_1, \sigma_2, \sigma_3$	Principle stresses	Δt_c	Critical time increment
$\epsilon_f, \epsilon_f^{pl}$	Equivalent fracture strain & equivalent plastic strain at fracture	l_{min}	Smallest element dimension in the system
R_0	Initial void radius	c_d	Speed of wave
$VGI_{critical}$	Critical void growth index	M_a	Connection moment that leads to yield mechanism in the angles
D	Damage variable	T_0	total initial posttensioning force
$\bar{\epsilon}_0^{pl}$	Equivalent plastic strain at Fracture initiation	k_b	Initial stiffness of the beam
C_1	Fracture initiation strain in pure shear	k_s	Initial stiffness of the strands
C_2	Fracture initiation strain in uniaxial tension	K_a, i	Theoretical initial stiffness of the angles
m	Hardening exponent of a power law for isotropic strain hardening	$V_{a, c}$	Shear force that leads to yield mechanism in the angles
K_p	Strength coefficient	M_p	Plastic flexural moment capacity of the angles

to undergo permanent residual deformation which rehabilitation of them is mostly not economically viable [6].

As a replacement to previous MRFs with welded connections, a new connection has been proposed to be used in structural systems, which is called posttensioned energy dissipation (PTED) that eliminates the residual deformation of the frame and minimizes the seismic damage. These connections include high strength steel posttensioned (PT) elements and energy dissipater (ED) devices. PT bars or strands that compress the beam against column flange are used to bring the structure back to its initial position following an earthquake, giving it self-centering (SC) capability. During cyclic movements of the frame ED devices experience plastic deformations and form plastic hinges which dissipate seismic energy. In these connections damage is confined to the energy dissipater components which are easily replaceable. Fig. 1(a) shows a typical PTED-MRF exterior connection. This connection has posttensioned high strength strands that run parallel to the beam web and through column flanges and bolted top-and-seat angles as energy dissipater devices. Fig. 1(b) depicts moment-rotation ($M - \theta_r$) response of a posttensioned connection where θ_r is relative rotation between beam and column. This flag shaped behavior is governed by gap opening (Δ_{gap}) and closing of the connection when it is subjected to cyclic loading. Initial stiffness of the connection prior to gap opening is the same as a welded connection. However after the decompression moment (M_a), the moment which initiates the gap opening, it is defined by stiffness of the angle and elastic stiffness of the strands. During loading, the angles yield and upon unloading, they will dissipate energy till eventually the connection

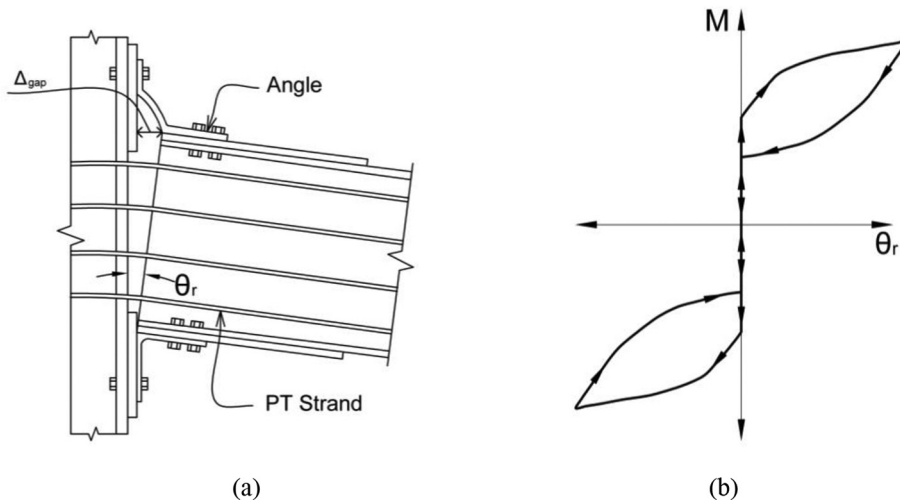


Fig. 1. PTED behavior, a) Deformation of a typical PTED connection [6], b) Moment rotation response [6].

is brought back to its plumb position ($\theta_r = 0$) [6].

The frames with PTED connections have many advantages that make them a superior and desirable alternative to the conventional MRFs. In PTED connections damage is confined to energy dissipater devices which are easily replaceable and main structural elements namely beams and columns stay elastic during the seismic loading and will not undergo any plastic deformations. Also no residual drift remains in the structure which considerably reduces post-earthquake repair costs and keeps the building functional and suitable for occupancy [6].

Ricles et al. [7,8] and Garlock et al. [6,9] experimentally studied the behavior of PTED connections with bolted top-and-seat angles under cyclic loading. The effects of different factors such as angle parameters, reinforcing plate and initial posttensioning force were investigated. Besides top-and-seat angles other energy dissipater devices have been proposed for PTED connections. Christopoulos et al. [10] developed a PETD connection with bars for energy dissipation. Chou et al. [11] proposed reduced flange plates (RFPs) which were welded to the column and bolted to the beam flange as energy dissipater devices. Another PTED connection with hourglass shaped steel cylindrical pins as energy dissipater elements were presented by Vasdravellis et al. [12]. Although PTED connections have been proven to be a proper alternative for semi-rigid connections there is still no guidelines in the current seismic design codes. Thus, further research studies are required to thoroughly investigate the application of these connections in buildings. In this regard, finite element (FE) analysis is an appropriate method that provides the possibility to analyze the behavior of PTED connections from different aspects that are hard to capture in an experimental test. Several FE studies have been carried out in order to investigate the effect of different factors on the performance of existing connections with SC capability. Chou and Lai [13] developed an analytical model of a PTED connection with beam bottom flange energy dissipaters. The behavior of the beams under posttensioned and flexural loading was investigated. Vasdravellis et al. [14] developed a FE model of a posttensioned connection with web hour glass pins. Parameters such as design procedure, details of the beam reinforcing, the beam and column size were investigated. Moradi and Alam [15] performed a FE analysis on a PTED connection with bolted top-and-seat angles which was experimentally tested by Ricles et al. [7]. They investigated the presence of reinforcing plates, the yield strength and strain hardening of the angles and the initial posttensioning force in the strands. Analytical results showed that the presence of beam flange reinforcing plates and increasing the amount of initial posttensioning force result in greater initial stiffness, moment capacity and energy dissipation.

The main purpose of this study is to provide a detailed finite element (FE) modeling procedure which can accurately capture the failure modes of PTED connection under cyclic loading. In this regard, three-dimensional FE models of three PTED connection specimens with bolted top-and-seat angles are developed. Full cyclic behavior of FE models are simulated using ABAQUS software. The three specimens experience different failure modes including beam local buckling, strand yielding and angle fracture. The explicit method has been used for means of analysis to prevent convergence difficulties caused by the fracture and extensive yielding in the models. The analytical results are verified based on the experimental data provided by Garlock et al. [6,16]. One of the applications of simulating failure modes is to investigate possible approaches to improve the behavior of member or members which undergo extensive damage which in turn might affect the global performance of the entire system. In this regard, a method has been recommended which reduce the fracture possibility in angles and also enhance the energy dissipation of these members. The material properties of the angles are replaced by LYP100 steel. LYP100 steel has normal yield strength of 100 MPa and has an excellent ductility (from now on it is referred to as LYP steel for the purpose of simplicity). Then models are subjected to the same analysis procedure and factors including lateral load-displacement responses, total energy dissipation, plastic energy dissipation and fracture initiation point of these connections are compared to those with angles made of ASTM A572 Grade50 steel (from now on it is referred to as A572 steel).

2. Development of FE models

2.1. Reference PTED connection

In this study, three PTED connection specimens studied by Garlock et al. [6] are chosen and their three-dimensional model is developed using non-linear FE analysis software ABAQUS [16]. Garlock et al. [6] experimentally tested six full scale interior PTED connections with bolted top-and-seat angles and high strength posttensioned strands under cyclic loading. They investigated parameters including initial posttensioning force, number of posttensioned strands and length of the reinforcing plates. The results indicated that up to 4% story drift main structural elements remain elastic and damage is limited to the angles.

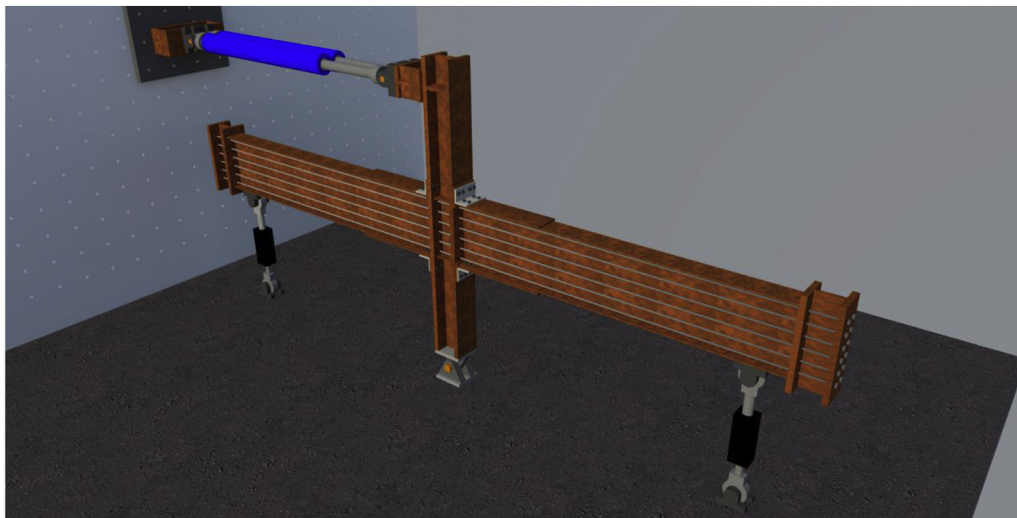
Table 1
Specimens details [6].

Specimen	No. of strands	Total posttensioning force (kN)	Length of the reinforcing plate (mm)	Limit state
36s-20-P	36	3149	1372	None
16s-45	16	3051	914	Strand yielding
20s-18	20	1526	914	Angle fracture

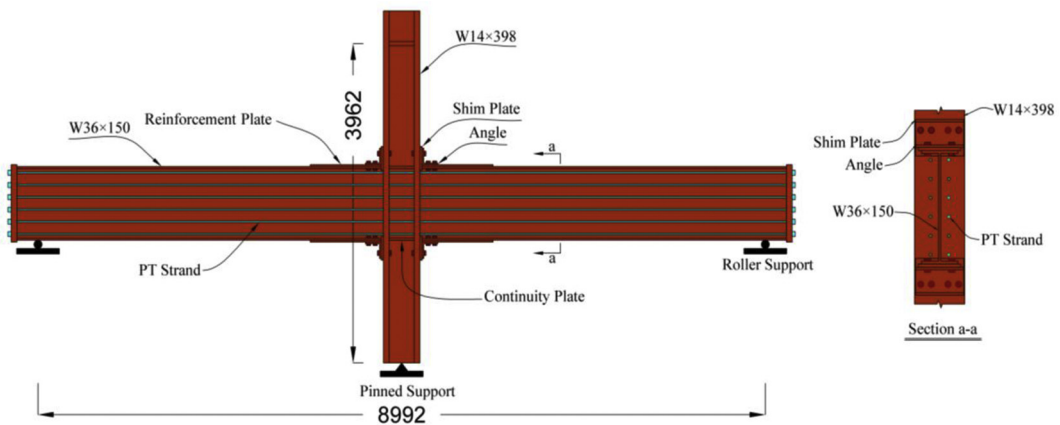
2.2. Geometry modeling

Specimen 36s-20-P, 16s-45 and 20s-18 are chosen for FE modeling. The specimens are basically the same in geometry with variation in number of strands and length of the reinforcing plates. Table 1 lists the details of the specimens. Total initial post-tensioning force in strands and length of the beam flange reinforcing plates are presented. Reinforcing plates are employed to prevent beam local buckling. Each specimen experiences separate limit states including beam local buckling, strand yielding and angle fracture. These three connection specimens are selected in order to cover all of the limit states in the experimental test and to reassure the precision of FE modeling. No limit state is listed for specimen 36s-20P since this specimen were supposed to experience limit state of angles fracture but at the end of test, angle fracture did not occur and test was terminated due to observation of buckling in the web of the beams. Further explanation will be presented in Section 3.1.

Fig. 2(a) illustrates the test setup of Garlock et al. [6] experimental study. The distance from one beam vertical support to the other is 8992 mm. The column height is equal to 3962 mm. All of the specimens are fabricated with W14 × 398 column and W36 × 150 beam sections. The connection have six levels of evenly spaced posttensioned strands on both sides of the beam web with an area of 140 mm² passing through the holes that are drilled in the columns with diameter of 44 mm. Four 8 × 8 × 3/4 angles with 406 mm width are placed on the top and bottom beam flanges. Two rows of two and one row of four A490 bolts connect the angle to the beam and column flange, respectively. Reinforcing plates with thickness of 25 mm and width of 356 mm are welded to the beam flanges. Furthermore, shim plates with 292 mm length, 406 mm width and 32 mm thickness are welded to the column flanges. One 19 mm thick doubler plate and two 25 mm thick continuity plates are placed at each side of the column. As it is shown in Fig. 2(a) the strands are anchored against short columns at the end of the beams. However, in the FE modeling, instead of simulating anchorage columns, two plates are considered at the end of each beam (Fig. 2(b)). This reduces the computational cost and does not affect the



(a)



(b)

Fig. 2. PTED frame setup, a) 3D view of Garlock et al. [6] experimental test setup, b) Test setup in FE modeling.

results.

Also to avoid any inaccuracy, the whole test setup is modeled and symmetry condition is not applied. All of the members are modeled using 3D deformable solid (continuum) elements which are available in ABAQUS library [16]. Solid elements can be used in complex non-linear analyses that include numerous contact surfaces, plasticity and large deformations [16].

2.3. Material properties

All of the components are made of A572 steel except for the bolts and strands which are made of A490 and A416 steel, respectively. Table 2 presents yield and ultimate stress of each member in accordance with material test conducted by Garlock et al. [6]. Posttensioned strands have Young's modulus (E) and the tensile capacity of 199Gpa and 266kN, respectively. Young's modulus of other members is defined as 200GPa. Poisson's ratio (ν) for all of the elements is taken as 0.3. In order to define stress–strain relationship for members, stress–strain curves of components which were obtained through tensile coupon tests, are employed [17].

The nominal stress σ_{nom} and nominal strain ϵ_{nom} are converted into linear true stress σ_{true} (Eq. (1)) and logarithmic plastic strain ϵ_{ln}^{pl} (Eq. (2)) so that they can be used as input parameters to define the elastoplastic behavior of the steel in the material modeling [14].

$$\sigma_{true} = \sigma_{nom}(1 + \epsilon_{nom}) \quad (1)$$

$$\epsilon_{ln}^{pl} = \ln(1 + \epsilon_{nom}) - \frac{\sigma_{true}}{E} \quad (2)$$

2.4. Failure modeling

Various research have been performed to simulate failure in steel connections. Fangfang et al. [18] performed finite element analysis on welded connection specimen between steel tube column and H-beam flange under monotonic tensile loading to predict ductile fracture using micromechanical fracture criteria which contained stress modified critical strain (SMCS) and void growth model. The analytical results showed high correlation with experimental results and the calibrated fracture criteria and simulation method could be used for modeling collapse. Amiri et al. [19] presented a method to predict ductile fracture in steel connection under large amplitude cyclic straining experience in earthquakes. The model was developed using an available model for predicting crack initiation in ultra-low cycle fatigue and was able to predict crack location, number of cycles needed for crack to be initiated and propagation track of crack. Fernandez-Ceniceros et al. [20] presented a refined finite element model for predicting ductile behavior of T-stub connection which included initial stiffness to the point of fracture. A parametric study was also conducted to examine the effect of damage parameters on the response of connection. Wang et al. [21] experimentally and analytically investigated the performance of beam-to-SHS column connections under progressive collapse. Three connection types including welded flange-weld web connection, welded flange-bolted web connection and welded flange-bolted web connection were tested and failure modes, load deformations responses were obtained. Then further details were studied through finite element modeling of the connection.

2.4.1. Beam local buckling

There two steps to accurately model buckling in structural members. First, buckling analysis is performed to obtain the buckling modes. Second, imperfection is defined for elements with respect to the buckling mode obtained in previous step and then nonlinear analysis is carried out. Using this method, it is possible to approximate the behavior of an element which experience buckling [22–25]. In this study, initial imperfection is not defined for the beam. It was shown in previous studies that when cyclic loading is applied to the model, due to accumulation of plastic strain in the member, the required imperfection for simulating the local buckling is provided [26,27]. Applying this method might not be conservative especially in studies with monotonic loading. It is better to perform parametric studies and obtain the exact amount of imperfection and apply imperfection in research which the main goal is to accurately capture buckling [26]. However, in this study beam local buckling in the specimen 36s-20-P is not the main failure mode and only signs of local buckling have been observed in the beam. Since this beam were supposed to be used in the next experiment the test was terminated to prevent further damage to the beam [17]. Also the cyclic loading provides the sufficient imperfection to model the local buckling. Therefore no further setup is employed to simulate the local buckling in beams.

Table 2
Material properties [6].

Item	σ_y (MPa)	σ_u (MPa)
Beam flange	362	498
Beam web	414	527
Reinforcing plates	397	574
Column flange	356	499
Column web	345	545
Angles	383	523
PT strands	1620	1900

2.4.2. Strand yielding

In previous studies, few research can be found which particularly investigate the failure of cables. Usually the behavior of cables had been captured within the range of low strains [28–30]. However, in this study to properly address the behavior of a PTED connection, modeling the failure mode of the strands should be taken into consideration. For this purpose, in this study the model which was employed by Judge et al. [31] has been used. In this model when the element reaches the maximum load, it loses its load bearing capacity. A maximum stress and strain is defined for the strand material which has been presented by Garlock et al. [17]. The strand manufacturing company has performed material tests on the strands and based on the load-elongation curve presented for these members, the yielding stress and strain of the strands is defined at 1600 MPa and 0.08. Also the ultimate yield strength is defined at stress of 1900 MPa and strain of 5.31%. As reported by Garlock et al. [17] throughout the testing of specimen 16s-45 none of the strands reached the ultimate force which was determined by the manufacturing company. Each strand contains seven wires and in this specimen four out of sixteen strands experience wire fracture. The strand forces in strands 30A, 29A, 28A and 28B reached 213kN, 227kN, 231kN and 231kN, respectively. The ultimate forces of strands in the experiment are estimated just before the fracture of wires in strands. To capture the limit state of strand yielding in specimen 16s-45 these forces in the aforementioned strands are considered based on the reported values.

Simplification has been made due to the full scale dimensions of the frame in this study. The strand consists of several wires wrapped in a covering, however in this study the strand is modeled as an integrated element. This modification leads to yielding of the whole strand when reaching to a certain load while in the experiment in similar situation one or some of the wires would have been fractured. Nonetheless, this modeling simplification is preferred since it significantly reduces the computational cost and is conservative.

2.4.3. Fracture modeling

As discussed earlier, the limit state that specimen 20s-18 experiences is angle fracture. In order to capture fracture in FE modeling, damage should be defined in material properties. In the last fifty years different methods have been suggested for modeling fracture. In a study by McClintock [32] it was determined that fracture strain is inversely dependent to the hydrostatic tension in plastic materials. In a study by Rice and Tracey [33] regarding spherical void growth, it was discovered that expansion rate of these voids is intensified by a coefficient of an exponential function of the stress triaxiality. Johnson and Cook [34] proposed a formulation for fracture initiation that also accounts for the effects of strain rate and temperature. After that, different theories were developed for modeling fracture and several studies were carried out regarding FE modeling of fracture. There are numerous studies that investigate the fracture modeling in structural steel in form of notched coupon specimen under monotonic and cyclic loading, nonetheless modeling fracture in full scale steel frame are rare.

Zhou and Jia [35] presented a damage index for crack initiation which accounted for the effects of damage accumulation. For verification of this criterion cyclic tension and compression test of notched bars were performed and results were analyzed with plasticity procedures of FE software. Fernandez-Ceniceros et al. [20] carried out numerical study to evaluate the hysteresis response of T-stub component from the initial stiffness until fracture point. An experimental and analytical study was performed by Wang et al. [21] to investigate the performance of beam-to-SHS column connection against progressive collapse. It was concluded that progressive collapse might be initiated due to fracture in beam of this connection.

According to the cyclic tests performed on the structural steel, as the plastic strain increases cracks are most likely to develop due to the ductile mode rather than fatigue. In this regard, the crack formation in a severe seismic event with large amplitude strain is a

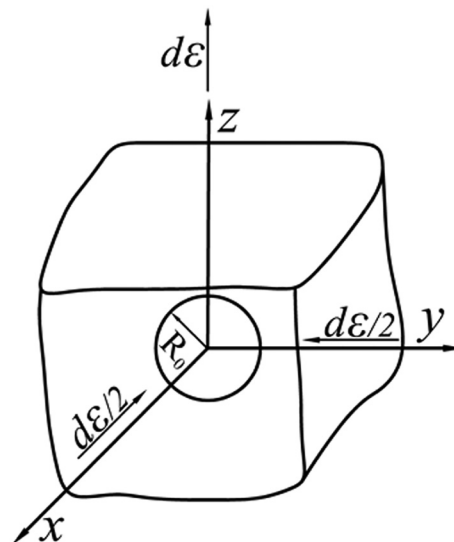


Fig. 3. Rice and Tracey void growth model [33],

result of ductile behavior of the steel. Research have determined that formation of ductile cracks is highly related to the stress triaxiality [36]. Although Rice and Tracey's [33] method has been presented many years ago, it has remained the favorite one among scholars and most of the studies which include modeling fracture in structural steel employ the similar or extended version of this formula. Rice and Tracey [33] formula for void growth rate is as follows (Fig. 3):

$$\frac{dR}{R} = 0.283 \cdot e^{\left(\frac{3}{2}\right)\left(\frac{\sigma_m}{\sigma_e}\right)} d\varepsilon_e = 0.283 \cdot e^{\left(\frac{3}{2}\right)\eta} d\varepsilon_e \tag{3}$$

In which R , σ_m , σ_e , η and ε_e are void radius, hydrostatic stress, equivalent stress, stress triaxiality and equivalent strain, respectively. Stress triaxiality η is defined as the hydrostatic σ_m to von Mises σ_e stress ration which are as follow (Fig. 4):

$$\eta = \sigma_m / \sigma_e \tag{4}$$

$$\sigma_m = \frac{1}{3}(\sigma_1 + \sigma_2 + \sigma_3) \tag{5}$$

$$\sigma_e = \frac{1}{\sqrt{2}}[(\sigma_1 - \sigma_2)^2 + (\sigma_1 - \sigma_3)^2 + (\sigma_2 - \sigma_3)^2]^{1/2}, (\sigma_1 > \sigma_2 > \sigma_3) \tag{6}$$

In a case that triaxiality could remain constant until fracture occurs, the relationship of fracture strain ε_f and stress triaxiality can be obtained through integrating Eq. (3) which is expressed in Eq. (7):

$$\varepsilon_f = \frac{\ln \frac{R_f}{R_0}}{0.283 e^{\left(\frac{3}{2}\right)\eta}} = VGI_{critical} \cdot e^{\left(-\frac{3}{2}\right)\eta} \tag{7}$$

The above criterion was first proposed by Panontin and Sheppard [37] in which ε_f , R_f and R_0 are the equivalent strain at fracture, void radius at fracture and initial void radius. $VGI_{critical}$ is a parameter which presents the critical value of void growth when the stress triaxiality is assumed to be constant. While the above formula have been used in previous studies [38] and leads to good results when triaxiality remains constant during loading, this assumption is not applicable in most cases. Therefore similar to fatigue problems, it is recommended to use the Miner's rule in fracture problems, too [39]. This rule states that damage can be linearly superimposed which results in the following formula [40]:

$$dD_{VGM} = \frac{d\varepsilon_e^{pl}}{\varepsilon_f^{pl}(\eta)} = \frac{d\varepsilon_e^{pl}}{VGI_{critical} \cdot e^{\left(-\frac{3}{2}\right)\eta}} \tag{8}$$

This formula is obtained assuming that the damage is only attributed to the equivalent plastic strain. In which ε_e^{pl} , ε_f^{pl} and D_{VGM} are equivalent plastic strain, equivalent plastic strain at fractures and damage variable in VGM. Although the above formula is capable of accounting for the effects of triaxiality change such as triaxiality change during cyclic loading, it also has the problem of not considering the shear failure. Shear failure might occur in a structure and ignoring it might lead to incorrect results in evaluation of structural elements. In a study by Hooputra et al. [41] a comprehensive solution was recommended for predicting failure on macroscopic stress and strains which accounted for different failure mechanisms such as shear fracture, ductile fracture and necking.

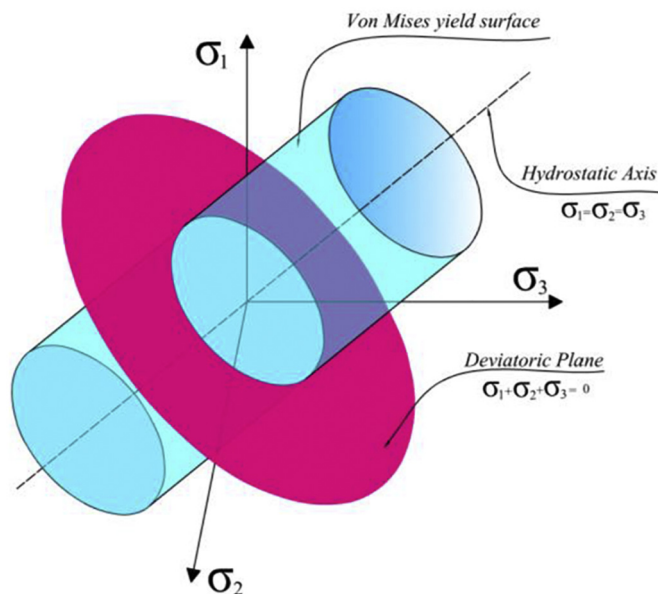


Fig. 4. Von Mises criteria.

While Hooputra's [41] method considers different kinds of failure, it contains seven free parameters. These parameters were not available for the structural steels in this study and therefore this method could not be employed.

Bao and Wierzbicki [42] performed an experimental and analytical study to investigate fracture ductility in different stress triaxialities. They obtained a relationship through experimental and numerical results that has three separate regions with slope disruptions. In the first region with negative triaxiality fracture is characterized by shear behavior. In the third region with high triaxiality fracture initiates due to the void growth and in the second region which is located between these two and have low triaxiality it is governed by both shear and void growth modes.

Drawing equivalent plastic strain versus triaxiality for previous theories such as Rice and Tracey's [33] and Johnson and Cook's [34] would give a diagram like the ductile fracture branch in Fig. 5 which continues along the dotted line.

However, for modeling fracture in Bao-Wierzbicki's [42] model two new geometric surfaces has replaced the dotted line which cover mixed mode and shear fracture. The Bao-Wierzbicki's [42] model is employed for simulating fracture in current paper which considers both shear and ductile fracture and is easy to calibrate. Since the current study intends to compare fracture formation for two different steel, this method is appropriate for this purpose.

The Bao-Wierzbicki [42,43] criterion that determines the fracture locus is defined as:

$$\bar{\epsilon}_0^{pl} = \begin{cases} \infty & \eta \leq -1/3 \\ C_1/(1 + 3\eta) & -1/3 \leq \eta \leq 0 \\ C_1 + (C_2 - C_1)(\eta/\eta_0)^2 & 0 < \eta \leq \eta_0 \\ C_2\eta_0/\eta & \eta_0 \leq \eta \end{cases} \quad (9)$$

where C_1 and C_2 are equal to fracture initiation strain in pure shear ($\eta = 0$) and uniaxial tension ($\eta = \eta_0 = 1/3$), respectively. Also $C_1 = C_2 \left(\frac{\sqrt{3}}{2}\right)^{1/m}$, where m is hardening exponent of a power law for isotropic strain hardening $\sigma = K_p \epsilon^m$ in which K_p is the strength coefficient. C_2 can be calculated using A_R , which is reduction in area of a uniaxial axisymmetric tensile specimen, by $C_2 = -\ln(1 - A_R)$ [44,45]. As mentioned earlier and in accordance with Eq. (5) there are separate regions that each one determines distinct fracture mechanisms. These regions are depicted in Fig. 5.

First region is for shear fracture, second for combination of shear and ductile fracture and third region is for ductile fracture governed by void growth. For triaxiality less than -0.33 which is located before region one, fracture does not occur [46]. Fig. 6(a) plots the equivalent plastic strain versus triaxiality for A572 and LYP steel. Bao-Wierzbicki's [42] model is calibrated for A572 and LYP steel based on studies by Novak [47] and Saeki et al. [48] respectively.

Damage is initiated when the fracture initiation criterion, $\omega_D = 1$, is met. In order to determine fracture initiation, ω_D employs the equivalent plastic strain and is equal to the integral of the ratio of the equivalent plastic strain to the critical equivalent plastic strain [41,44]. This criterion is expressed as follows:

$$\omega_D = \int \frac{d\bar{\epsilon}^{pl}}{\bar{\epsilon}_0^{pl}(\eta)} = 1 \quad (10)$$

The equivalent plastic strain $\bar{\epsilon}^{pl}$ is calculated using Eq. (11):

$$\bar{\epsilon}^{pl} = \bar{\epsilon}^{pl}_0 + \int_0^t \sqrt{\frac{2}{3} \sum_{i=1}^n \dot{\epsilon}_i^{pl} \dot{\epsilon}_i^{pl}} dt \quad (11)$$

In which $\bar{\epsilon}^{pl}_0$ shows the equivalent plastic strain at the time of $t = 0$, and $\dot{\epsilon}_i^{pl}$ is the plastic strain rate during the time increment. ω_D increases as expressed in Eq. (12) in each increment:

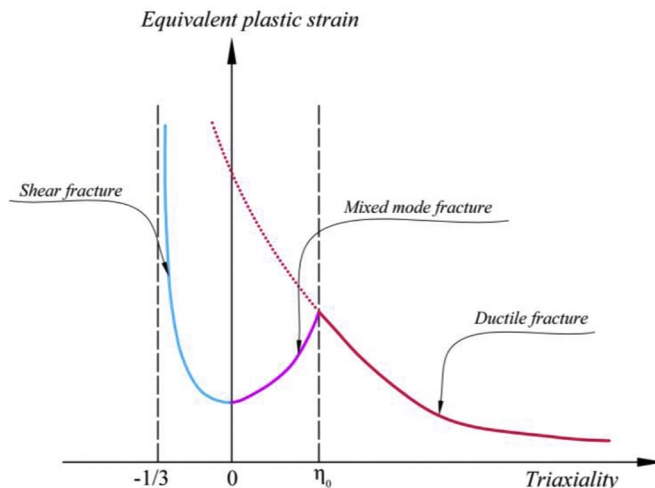


Fig. 5. Bao-Wierzbicki's model.

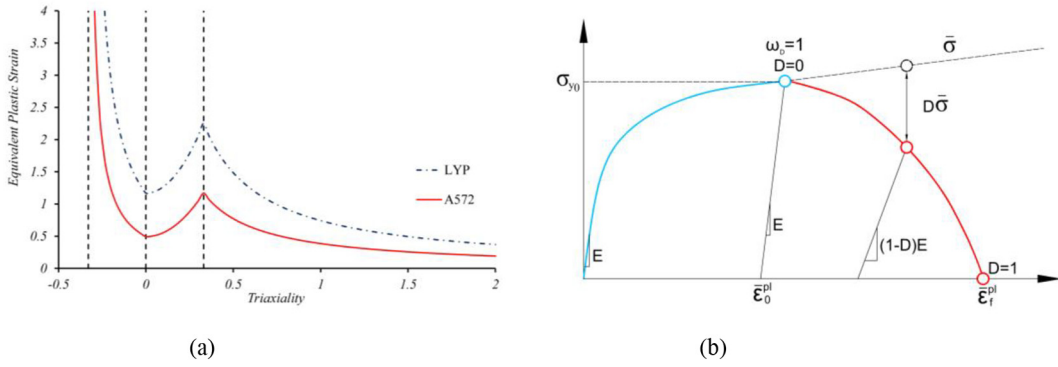


Fig. 6. Fracture modeling, a) B-W fracture locus for A572 and LYP steel b) Damage evolution Diagram [16].

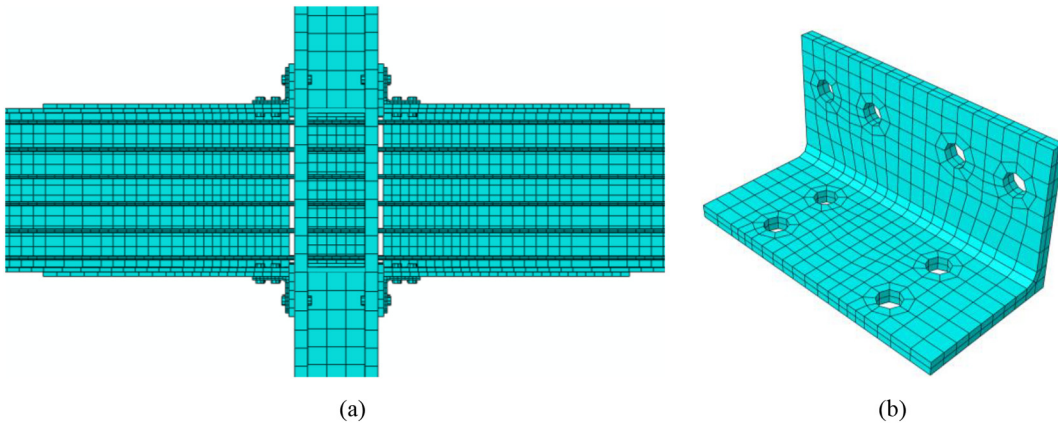


Fig. 7. Meshing details of specimen 36s-20-P; a) Panel zone, b) Angle.

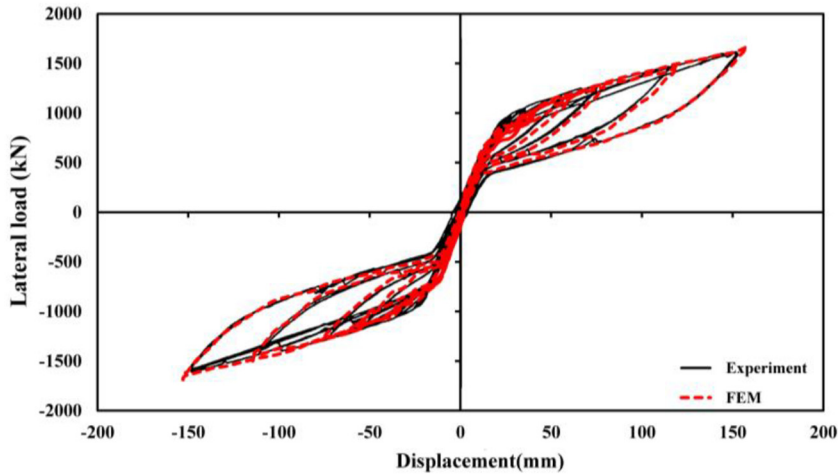


Fig. 8. Comparison of experimental and analytical lateral load-displacement responses in specimen 36s-20-P [17].

$$\Delta\omega_D = \frac{\Delta\bar{\epsilon}^{pl}}{\bar{\epsilon}_\delta^{pl}(\eta)} \geq 0 \tag{12}$$

The material behavior after damage initiation is defined in damage evolution which describes the rate of material stiffness degradation. Fig. 6(b) indicates stress-strain curve of elastic plastic material. D is the damage variable which increases monotonically with equivalent plastic displacement and is associated with softening of yield stress and degradation of elasticity [16]. The point $D = 0$, shows the onset of damage (Fig. 6(b)). Damage evolution is defined with \bar{u}^{pl} which is expressed as follows [16]:

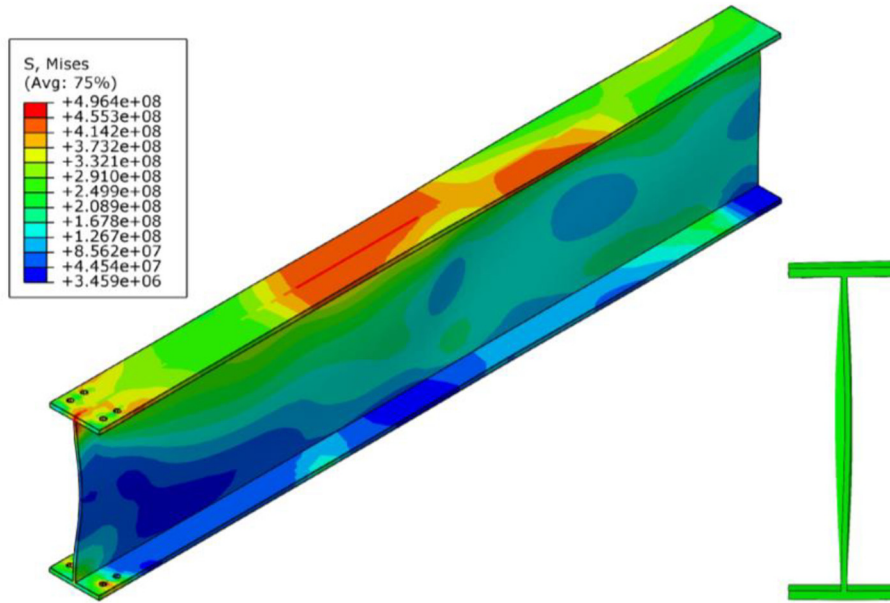


Fig. 9. Beam local buckling in FE model of specimen 36s-20-P at 4% story drift (in 3D view of the beam the scale factor in X direction is multiplied by four).

$$\bar{u}^{pl} = L\bar{\epsilon}^{pl} \quad (13)$$

Before the initiation of damage \bar{u}^{pl} equals zero and after that it equals to Eq. (13). Where L is the characteristic length of the element which is defined as cubic root of the integration point volume in current 3D model [16].

When the damage variable reaches its final value of 1 ($D = 1$), the material has lost its entire load bearing capacity and has failed completely (Fig. 6(b)). In current FE model fracture is simulated through elimination of the each mesh upon reaching $D = 1$.

2.5. Contact surfaces

To define the contact behavior between welded components, tie constraint is used. A surface-based tie is employed to fully constrain relative displacement between two separate surfaces. It utilizes a master-slave formulation. Tie constraint prevents nodes of the slave surface from separating or sliding toward master surface. Since welding parts do not undergo any damage during the experiment, using surface-based tie instead of modeling welds does not influence the accuracy of FE analysis and reduces the computational time. To simulate the interaction between other components, contact formulation with general contact algorithm is used. It provides the possibility to assign contact between many or all of the regions in a model with an individual interaction which makes it faster to define contacts in models with complex geometries and large number of contacting surfaces. Surface smoothing is also assigned which improves the accuracy of contact stress and pressure for curved surfaces such as bolts and strands in current modeling [16]. Tangential and normal behavior is considered between contacting surfaces. Normal behavior is defined as hard contact to avoid penetration of two adjacent surfaces. The tangential behavior between bolts shank and bolts hole and strands and strands hole is considered frictionless. The tangential behavior between other contacting surfaces is applied by penalty method. Friction coefficient of 0.35 is employed in accordance with AISC provisions (2005) [49].

2.6. Boundary condition and loading

As shown in Fig. 2(b), the beams and column have roller and pin support, respectively. To assign support condition to beams and column, rigid body constraint is employed. In order to prevent out of plane displacement of beams under cyclic loading, lateral displacement is constrained. Pretension force in bolts and strands is produced using predefined field tool. Initial post tensioning force of strands and bolts were converted to stress as required for the input of aforementioned tool.

In the experimental study cyclic loading was applied to the test setup at top of the column by two actuators [6]. As mentioned by Garlock et al. [6] the loading protocol was in accordance with SAC (SAC1997) and consisted of “six cycles at $u = 0.375$, 0.50, and 0.75%, four cycles at $u = 1.0\%$, and two cycles at $u = 1.5$, 2, 3, and 4% drift” [50]. In FE modeling, loading is applied as displacement to the loading point at top of the column flange as demonstrated in Fig. 2(b). Since damage is defined for specimen 20s-18, it is subjected to full cyclic loading history to account for the effects of equivalent plastic strain (PEEQ). However, each loading cycle is only applied once to specimens 16s-45 and 36s-20-P to decrease the computational time.

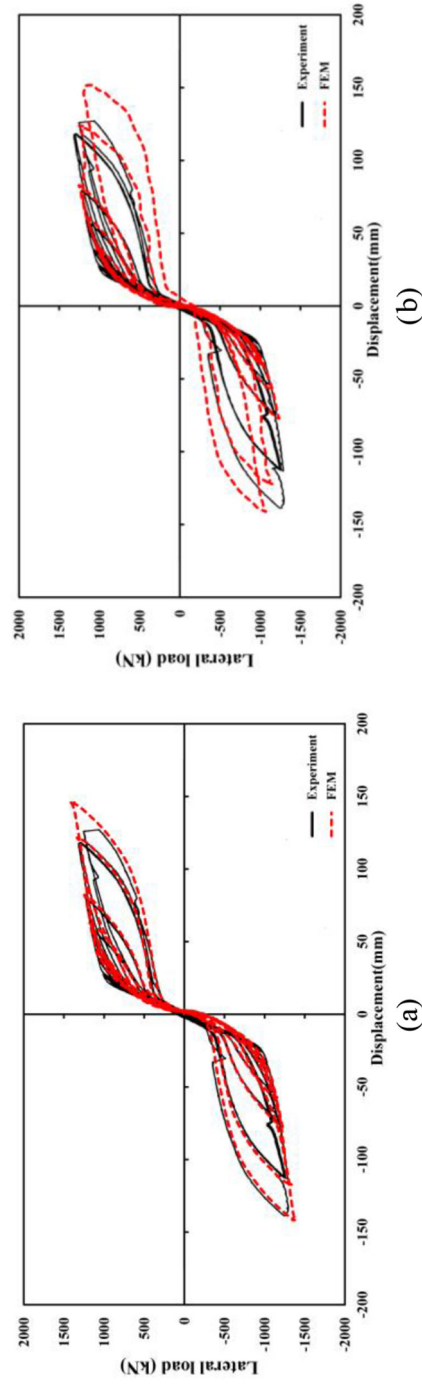


Fig. 10. Comparison of experimental and analytical lateral load-displacement responses in specimen 16s-45 [17]; a) (without strength degradation), b) (with strength degradation).

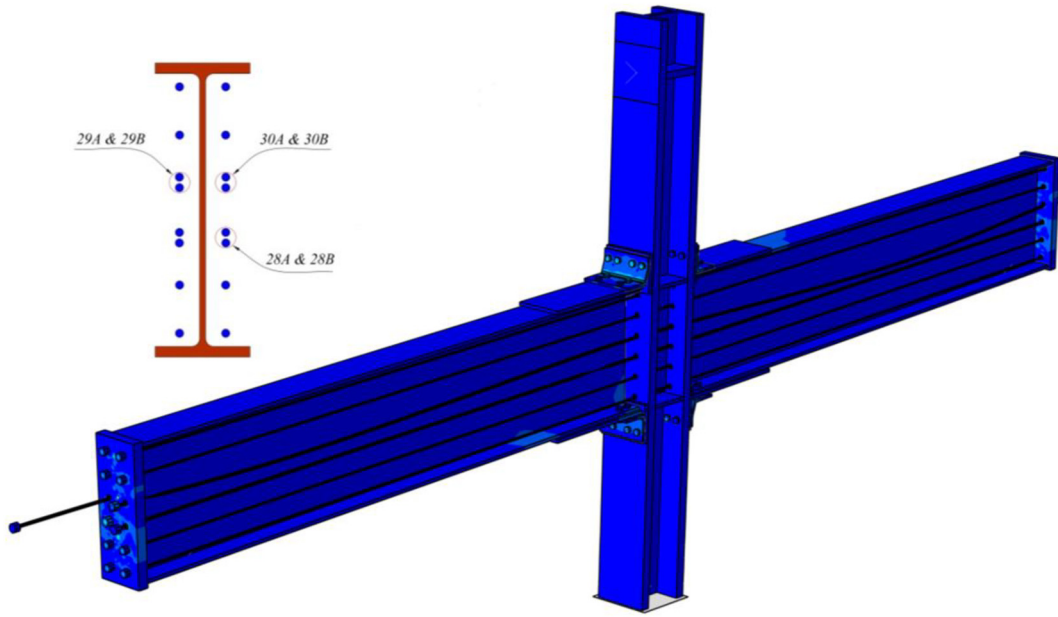


Fig. 11. Strand failure in specimen 16s-45 at 3.6% story drift in FE model and the schematic figure of damaged strands in experiment.

2.7. Analysis method

The explicit procedure is employed for the analysis. Unlike the standard procedure, this non-linear analysis method determines the solution without iterations and convergence checking. Ignoring the damping matrix, the equilibrium dynamic equation would be as follows:

$$M\ddot{u}_{(j)} + F_{(j)} = R_{(j)} \tag{14}$$

In which M , F and R are the mass matrix, internal load vector and external load vector, respectively. The central difference integration method is used to calculate the parameters at each increment. Using the acceleration at t_j which is a known value and can be computed using the Eq. (15), the velocity at $t_{j+\frac{1}{2}}$ and the displacement at t_{j+1} can be calculated through Eqs (16) and (17) [16]:

$$\ddot{u}_{(j)} = M^{-1} \cdot (R_{(j)} - F_{(j)}) \tag{15}$$

$$\dot{u}_{(j+\frac{1}{2})} = \dot{u}_{(j-\frac{1}{2})} + \frac{\Delta t_{(j+1)} + \Delta t_{(j)}}{2} \ddot{u}_{(j)} \tag{16}$$

$$u_{(j+1)} = u_{(j)} + \Delta t_{(j+1)} \dot{u}_{(j+\frac{1}{2})} \tag{17}$$

where \ddot{u}_j is the acceleration vector at the beginning of the increment, Subscript j indicates increment number and the $j + \frac{1}{2}$ and $j - \frac{1}{2}$ are the mid increment values.

The explicit analysis is stable when each increment of the procedure is small enough to satisfy the conditions in Eq. (18). Eq. (18) shows the requirements for a system with and without considering the damping factor.

$$\Delta t = \frac{2}{\omega_{max}} (\sqrt{1 + \xi_{max}^2} - \xi_{max}), \Delta t \leq \frac{2}{\omega_{max}} \tag{18}$$

In which ω_{max} is maximum eigenvalue of the system and ξ_{max} is the corresponding damping ratio. In order for the time increment Δt to meet the requirements in Eq. (19), it should be less than the critical time increment Δt_c which is as follows [16]:

$$\Delta t \leq \Delta t_c = \frac{l_{min}^e}{c_d} \tag{19}$$

where l_{min} is the smallest element dimension in the system and c_d is the speed of wave moving through material.

The explicit procedure is capable of analyzing high speed dynamic and large nonlinear problems and is also a suitable method for solving problems which include numerous contact elements and experience high discontinuities such as buckling and fracture [16].

The current finite element models contain large number of elements and contact surfaces. They also experience local buckling and fracture. Therefore the explicit method is chosen as the analysis method, since it solves this kind of problems more efficiently and reduces the computational costs.

Various analysis steps are defined so that changes in the loading can be captured more easily. In the first step gravity load and

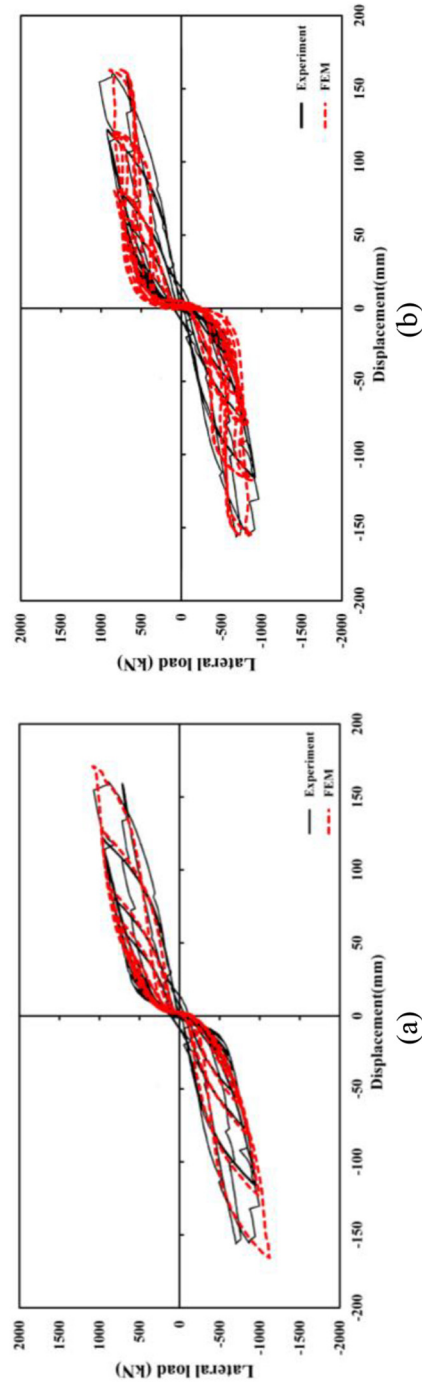


Fig. 12. Comparison of experimental and analytical lateral load-displacement responses in specimen 20s-18 [17], a) (without damage), b) (with damage).

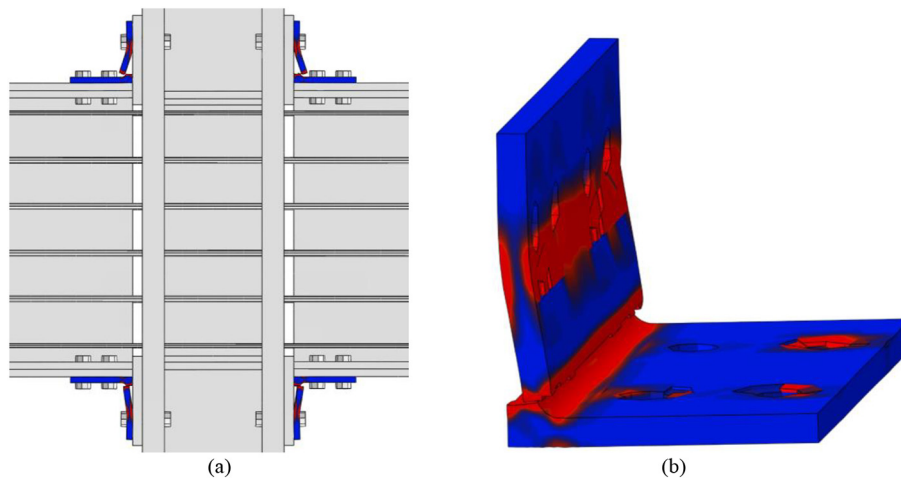


Fig. 13. Limit states; a) Angle fracture in specimen 20s-18(connections), b) Angle fracture in specimen20s-18(upper right angle).

pretension force in the bolts and strands are applied. After that, cyclic loading is applied through several steps with small enough durations so that the load can be applied gradually which improves the correlation between experimental and FE results.

2.8. Mesh selection

The specimens are meshed by 3D hexahedral element C3D8R (8-node linear brick) with reduced integration and hourglass control available in ABAQUS library [16]. Although hexahedral elements are hard to be adapted in models with complex geometries, by discretizing the components to smaller regions using partitions, these elements can be used. A good mesh of C3D8R elements can present efficient solution of equal precision at less computational cost [16]. A mesh study is carried out to find the mesh sizes that provide sufficient accuracy. Finer meshes are defined near the panel zone that experiences more variation in stress and strain and also for the angles that undergo significant yielding. The quality of meshes for all of the elements is verified using verify mesh tool. Fig. 7 shows meshing details of the panel zone and angles in specimen 36s-20-P.

3. FE analysis results

FE models of three specimens that were experimentally tested by Garlock et al. [6] were developed. Correlation study is presented here which contains comparing the lateral load displacement curves and failure modes obtained from the FE models with the ones from experimental specimens.

3.1. Specimen 36s-20-P

Fig. 8 plots lateral load-displacement responses of specimens 36s-20-P, obtained from FE analysis along with that of experimental study [17]. The lateral load and displacement are measured at the point of load application at top of the column flange. It can be seen that FE modeling has adequate accuracy and can well predict the stiffness, yielding point and strength of the specimen.

In the experiment, specimen 36s-20-P was subjected to up to 4% story drift and was anticipated to experience angle fracture as its limit state; however, after two and half cycles of 4% drift the angle fracture did not occur and test was stopped due to observation of buckling in the beam web [6]. Fig. 9 indicates the beam web buckling at 4% story drift in FE simulation and its von Mises stress distribution. In the experimental study beam web buckled which had a single wave with an amplitude of 6.35 mm [17]. In FE model the single wave in the beam web has amplitude of 9 mm.

3.2. Specimen 16s-45

Two FE models are developed for specimen 16s-45. Fig. 10(a) illustrates the lateral load-displacement response of FE model without considering the strength degradation in the strands. Since this specimen experience limit state of strand yielding strength degradation is defined in material properties of strands in another FE model in accordance with values reported by Garlock et al. [17] and the results is shown in Fig. 10(b). As it is shown this FE model shows more strength degradation than the experimental specimen (Fig. 10(b)). This is due to this reason that in the experiment, only one or two wires fracture in the strands that experience wire fracture. Nonetheless, in the FE simulation wires are not modeled and the strand is simulated as an integrated element. Failure of strands is defined in the FE model in a way which upon reaching the ultimate force, the strands are not able to bear loads anymore and therefor undergo extensive deformation.

Fig. 11 depicts the deformed shape of this specimen at 3.6% story drift and the location of the damaged strands. In the

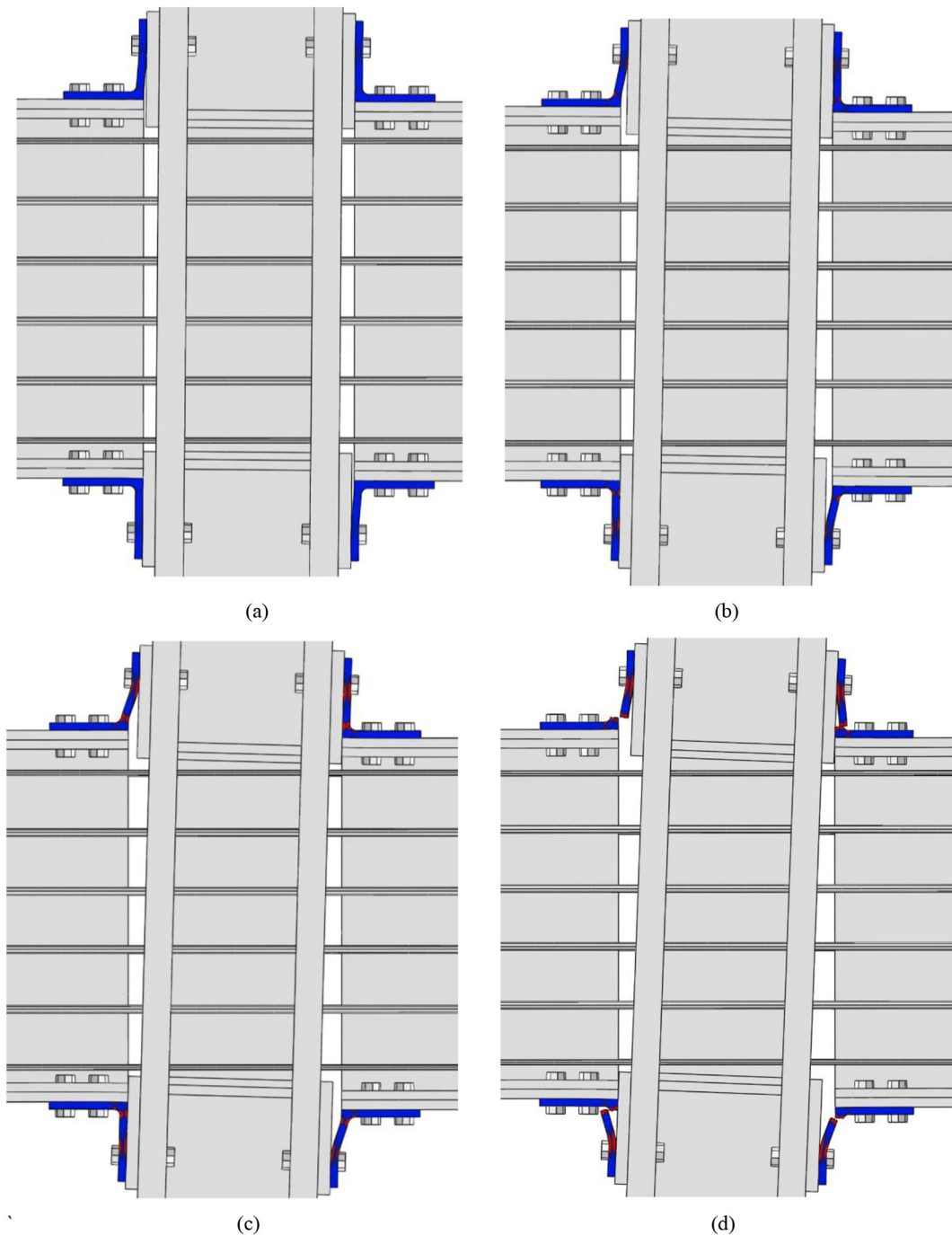


Fig. 14. Damage in angles of specimen 20s-18 at different drifts, a)1%, b)2%, c)3%, d)4%.

experimental study specimen 16s-45 was subjected to up to 3.6% story drift and was expected to have the limit state of strand yielding [6].

During the test one wire on strand 30A fractured at 2% drift, one wire on strand 29A fractured at 3% and three wires on strand 28A and 28B fractured at 3.5% drift [17]. In the FE model strand 30A, 29A, 28A and 28B reach their ultimate loads at cycle of 2% drift, 3% drift, 3.6% drift and 3.6% drift respectively.

3.3. Specimen 20s-18

As discussed before, damage is simulated through elimination of mesh elements. This will affect the strength of the connection. In

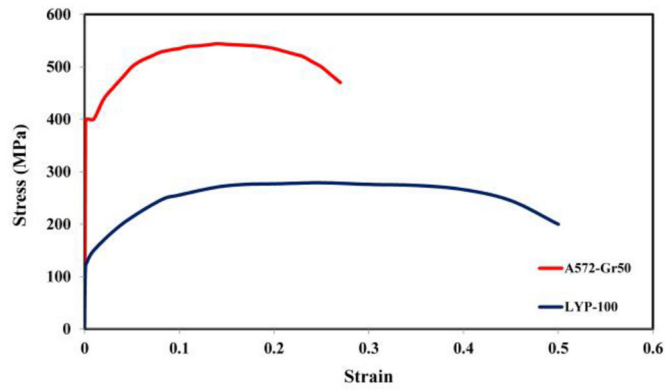


Fig. 15. Comparison of stress-strain curves of A572 Grade50 and LYP100 steel [17,57].

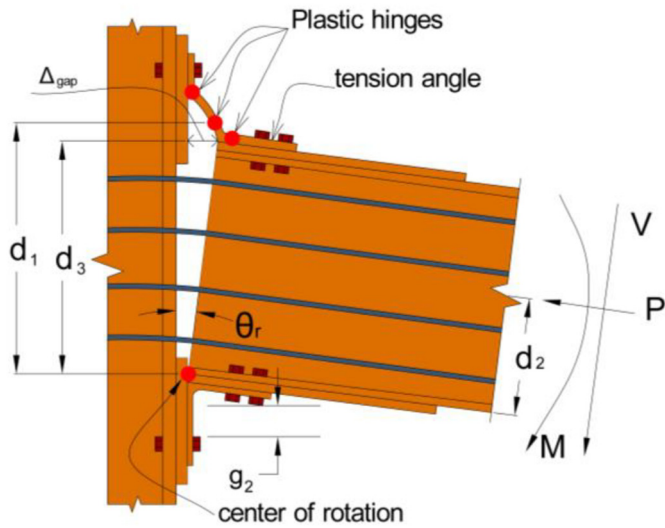


Fig. 16. Parameters of a decompressed PTED connection [58]

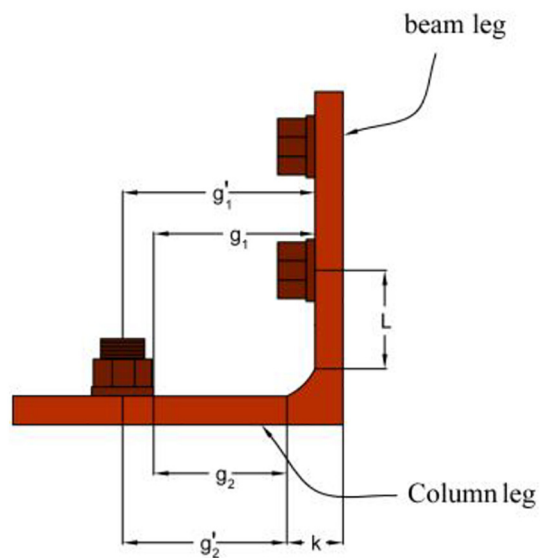


Fig. 17. Angle parametrs [9].

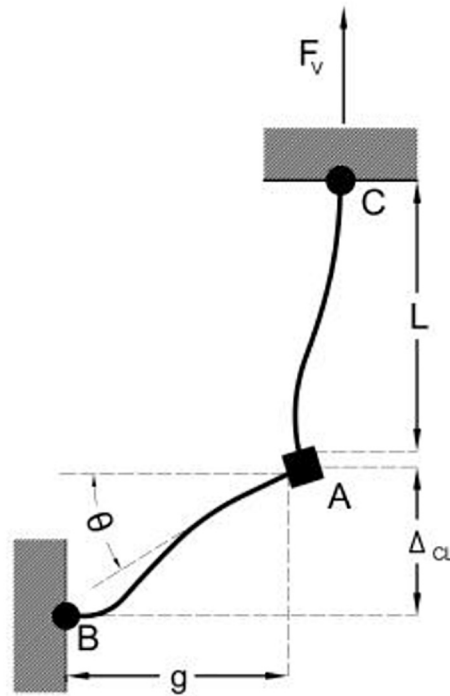


Fig. 18. Free body diagram of angle deformed shape [9].

this regard, two FE models are developed for specimen 20s-18 with and without considering damage, therefore it is ensured that damage properly works. Comparing Fig. 12(a) and (b) indicates that, the model with damage is able to capture the strength degradation which is not evident in model without damage.

In the experimental study specimen 20s-18 experienced the limit state of angle fracture. All four angles fractured after two cycle of 4% story drift. In order to simulate fracture in the FE model, complete loading history is applied to the specimen so that the effects of PEEQ are considered. Damage is defined in material properties of the angle in accordance with Section 2.4.3. Fig. 13(a) demonstrates four angles at the end of the second cycle of 4% story drift. In accordance with the experiment, all of the angles are fractured in the fillet of the leg which is connected to the column.

Fig. 13(b) gives a closer look at one of the angles with damage initiation criterion. This criterion represents ω_D . Fig. 14 shows the damage development in angles of specimen 20s-18 in drifts of 1%, 2%, 3% and 4%.

4. Application of LYP steel in top-and-seat angles

Low yield point (LYP) steel is a new type of steel which was first developed in Japan to be used in damping members and devices [48]. When a structure is subjected to earthquake, the imposed damage can be reduced by using an advanced material in the members which are allocated to dissipate energy. These members are able to yield before other structural elements and therefore dissipate earthquake energy through their plastic deformation [51]. Having low yield strength, great deformation capability and low-cycle fatigue performance make the LYP steel a suitable option for the aforementioned advanced material [52,53]. Several studies have been conducted on the application of LYP steel in seismic structures. Wang et al. [51] experimentally developed a constitutive model of LYP steel SLY100 and used it in analytical modeling of buckling restrained braces (BRBs). In an experimental study Nakashima [54] investigated the hysteretic behavior of shear panel dampers constructed with LYP steel. Chen and Jhang [55] performed series of experimental research to investigate seismic resistant behavior of LYP steel shear wall.

In this study LYP steel is employed as a replacement to A572 steel in energy dissipater devices of PTED connection models. Fig. 15 compares stress-strain curves of A572 steel and LYP steel. As it can be seen LYP steel does not have a visible yielding plateau and yielding strain is one fourth of the structural steel A572. LYP steel has much higher strain hardening in the plastic range and the same Young's modulus as the conventional structural steel. LYP steel has a low yield ratio (F_y/F_U) of 0.34 which enables the structures with this kind of steel to access larger plastic zone [56].

4.1. Recalculation of angle dimensions

To investigate the effects of using LYP steel in energy dissipater devices, on the responses of a PTED connection, the material properties of LYP steel is assigned to the top-and-seat angles in accordance with stress-strain relationship curve as shown in Fig. 15.

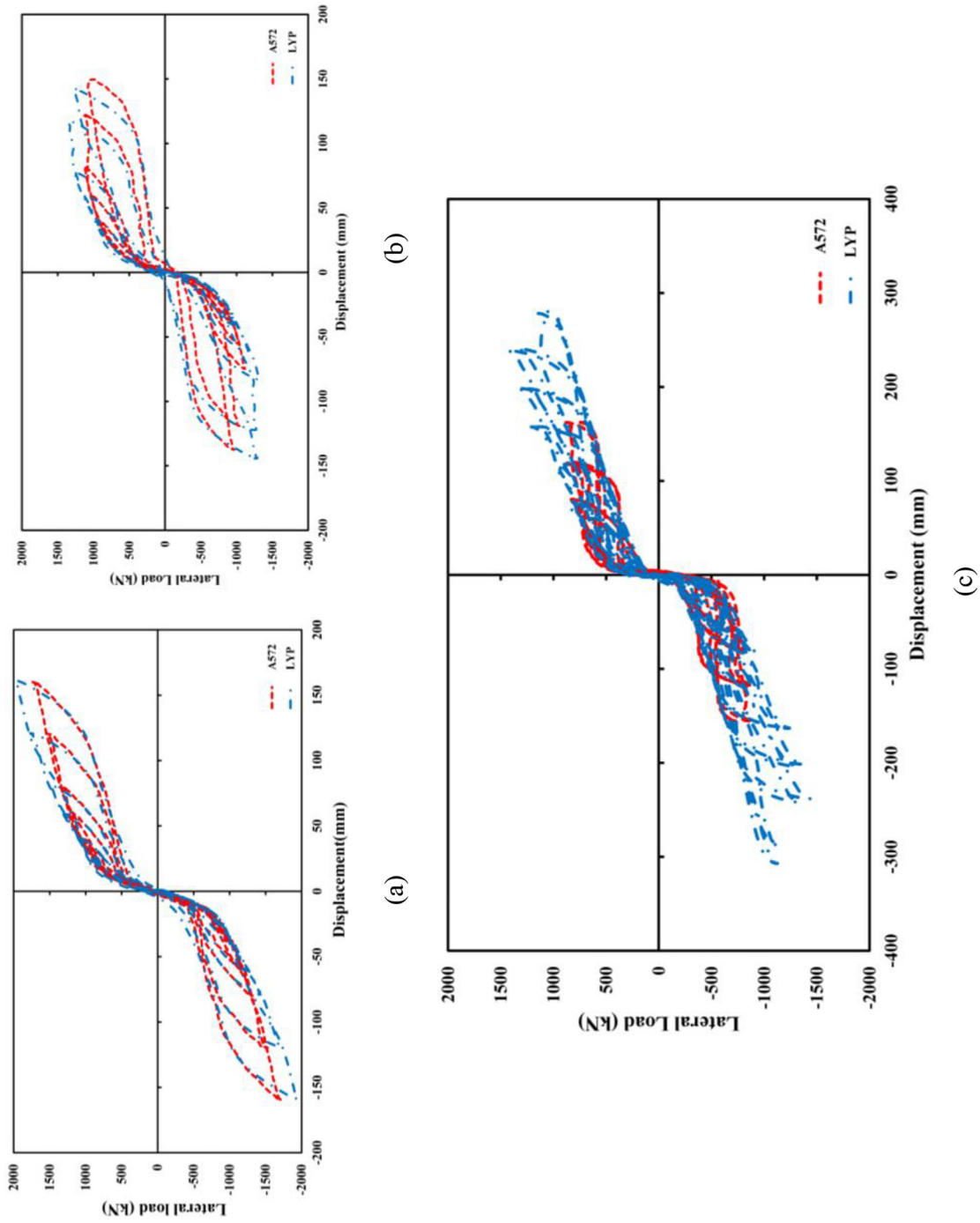


Fig. 19. Comparison of lateral load-displacement response in specimens with A572 and LYP steel angles; a)36s-20-P, b)16s-45, c) 20s-18.

Table 3
Connection parameters for A572 [17] and LYP steel angles.

Specimen	d ₁ (mm)	d ₂ (mm)	d ₃ (mm)	L (mm)	K (mm)	g ₁ (mm)	g ₂ (mm)	g ₁ ' (mm)	g ₂ ' (mm)
36s-20-P (A572steel)	971.8	455.9	936.8	41.2	34.9	88.1	72.2	117.4	101.5
36s-20-P (LYP steel)	979.9	455.9	936.8	33.1	43.1	69.1	64.1	98.4	93.4

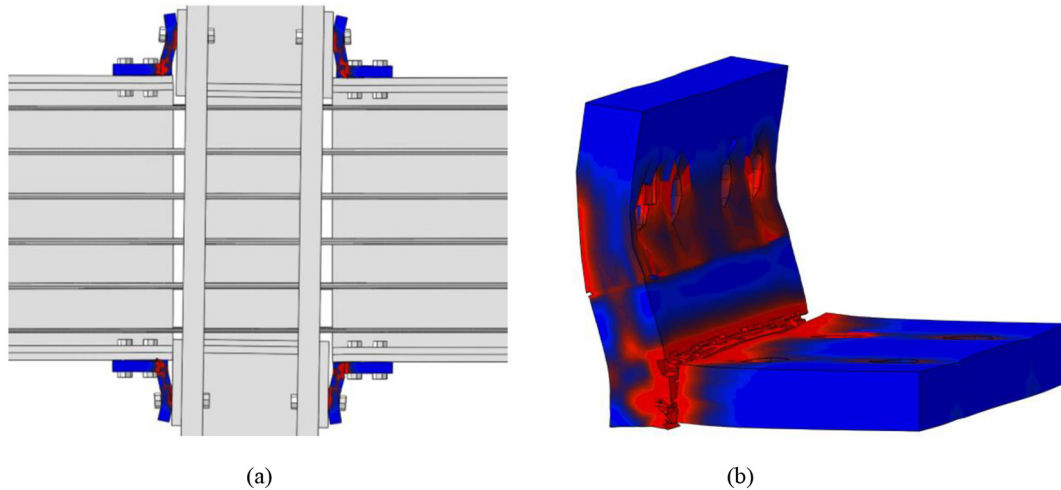


Fig. 20. Angle fracture in specimen 20s-18 with LYP angles, a) Connections, b) Upper right angle.

The geometry of the angles is recalculated so that they have the same yielding mechanism as that of the angles made of A572 steel. The connection moment under which angles start yielding is calculated using a formulation proposed by Garlock et al. [58]:

$$M_a = d_2 T_0 + d_1 V_{a,c} \left(1 + \frac{2d_2^2}{K_{a,i} d_1 d_3} \left(\frac{k_b k_s}{k_b + k_s} \right) \right) \tag{20}$$

In this formulation d₁, d₂, d₃ are distances which are shown in Fig. 16, T₀ is total initial posttensioning force, k_b is the initial stiffness of the beam and k_s is the initial stiffness of the strands. K_{a, i} Presents the theoretical initial stiffness of the angles and contains stiffness associated with bending and shear deformation. The formula for calculation of K_{a, i} can be found elsewhere [9]. V_{a, c} is the shear force that leads to yield mechanism in the angles which is presented as follows [9]:

$$V_{a,c} = \frac{2M_p}{g_{eff}} \tag{21}$$

Where M_p is plastic flexural moment capacity of the angles. g_{eff} is an angle parameter which in here is taken equal to g₂' , since it gives more accurate ratio of experimental to theoretical shear force.

Angle parameters are shown in Fig. 17. Free body diagram of angle deformed shape is demonstrated in Fig. 18.

Due to the geometrical issues of the connection configuration, merely angle thickness can be altered to compensate for changes in its material properties. The new thickness of the angle with LYP steel is calculated using Eq. (20) and setting M_{a, A572} = M_{a, LYP100}. The obtained angle thickness is slightly > 2 times the thickness of A572 angle. The angle thickness is considered to be exactly 2 times the thickness of A572 angle and the FE model is developed based on this assumption. The lateral load-displacement responses of FE models with LYP angles are compared to those with A572 angles in the next section (Fig. 19). It can be seen that both models have the same initial stiffness and yielding point.

Connection parameters for specimen 36s-20-P which are required to satisfy Eq. (20) are listed in Table 3 for both kinds of steel. Connection parameters shown for angle with LYP steel are considering the thickness of 38.1 mm (2 times the thickness of A572 angle).

4.2. Results and discussion

The analysis results for PTED connection models with LYP angles are presented here. Fig. 19 compares Lateral load-displacement responses of PTED connection models with angles made of A572 and LYP steel. It can be seen that the angles with new dimension and material properties have the same initial stiffness and yielding point. Specimen 36s-20-P and 16s-45 are subjected to the same loading procedure.

Specimen 20s-18 is subjected to more loading cycles to evaluate the performance of LYP angles. In the experimental specimen

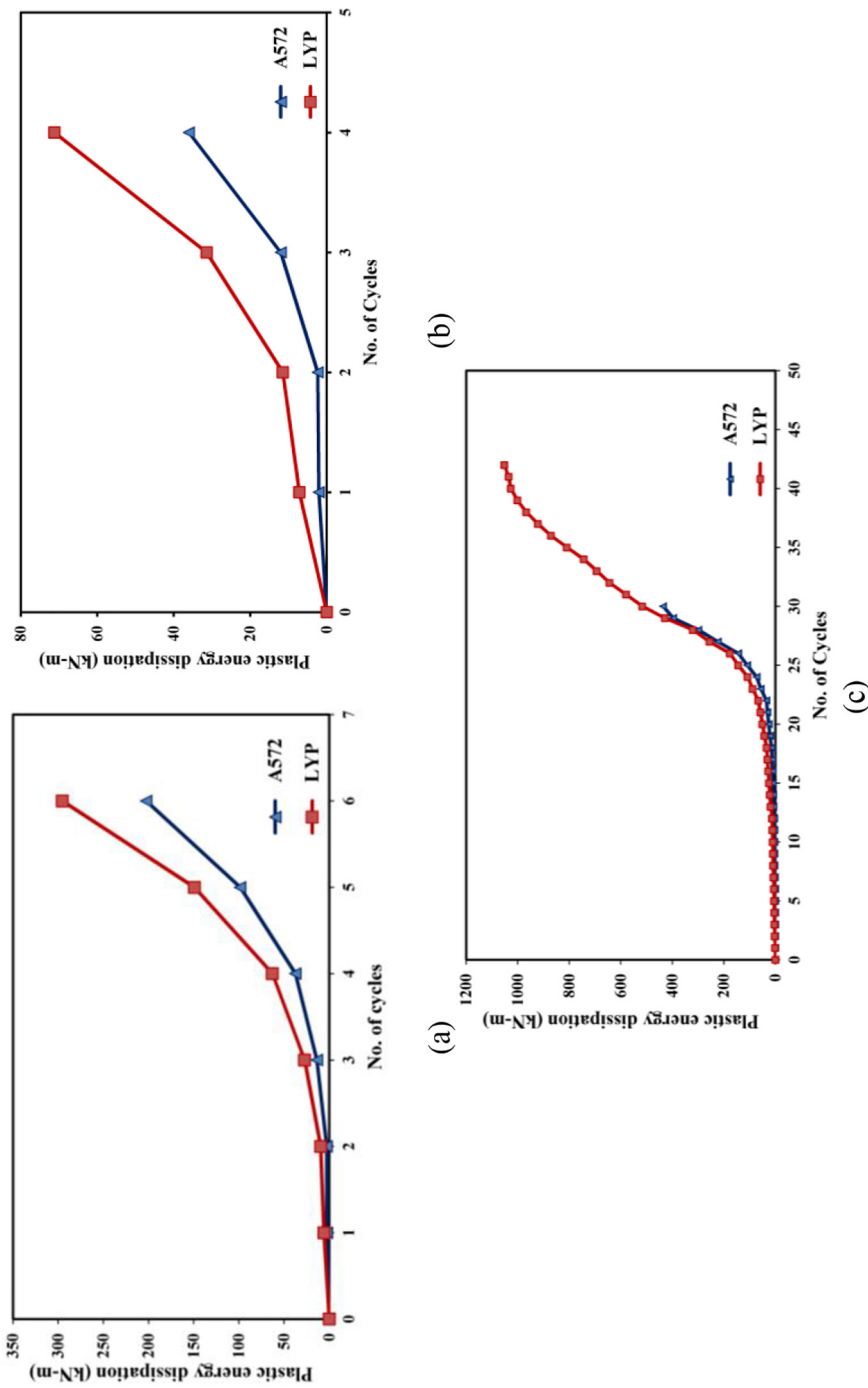


Fig. 21. Comparison of plastic energy dissipation versus cycle number in specimens with A572 and LYP steel angles; a) 36s-20-P, b) 16s-45, c) 20s-18.

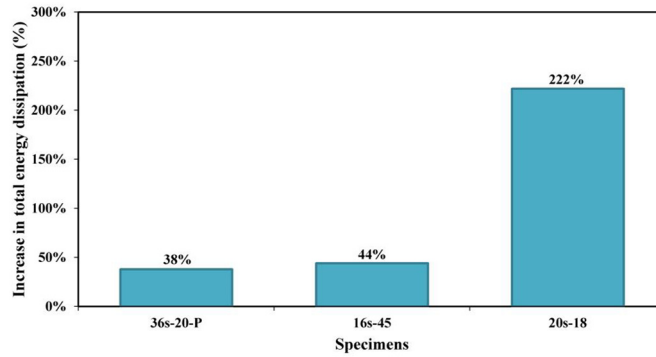


Fig. 22. Increase in total energy dissipation of specimens using LYP steel.

20s-18 with A572 steel, four angles fractured after two cycles of 4% drift. However FE model with LYP angles is subjected to extra loading cycles with increments in drift of 1% and performing two cycles at each drift which is in accordance with SAC loading protocol [50]. The loading protocol is continued until failure of the angles. Specimen 20s-18 endured 6% drift but all of the angles were completely fractured after one cycle of 7% drift.

Fig. 20(a) shows the specimen 20s-18 with LYP angles after the first cycle of 7% drift. All of the angles are completely fractured from their fillet. Fig. 20(b) demonstrates upper right angle of the connection. It was mentioned earlier that the most important merit of the LYP steel is its remarkable energy dissipation capability. Therefore, total and plastic energy dissipation of the PTED connection with A572 and LYP steel are compared. Since in PTED connection angles dissipate energy through plastic deformation, comparison of plastic energy dissipation of angles with two kinds of steel has significant importance.

Fig. 21 plots plastic energy dissipation per number of cycles. In accordance with Fig. 21, using LYP steel in the angles increases the plastic energy dissipation by 45%, 97% and 141% in specimens 36s-20-P, 16s-45 and 20s-18, respectively.

Difference in plastic dissipation is lower in specimens 36s-20-P and 16s-45. These specimens experience similar limit states in the same number of loading cycles for both kinds of steel. Plastic energy dissipation of specimen 16s-45 was subjected to significant discontinuity after cycle at 2% drift when the first strand experienced yielding. In this regard for this specimen plastic energy dissipation is compared for the first four cycle until cycle at 2% drift (Fig. 21(b)). This difference is more considerable in specimen 20s-18. The limit state of specimen 20s-18 with A572 steel is angle fracture. Since the FE model of specimen 20s-18 with LYP angle does not experience angle fracture with the same number of loading cycles as the one with A572 angle, extra loading cycles are applied to the model until its fracture. Therefore there is huge difference between plastic energy dissipation of this specimen. As shown in Fig. 21(c) plastic dissipation curve of specimen 20s-18 with both A572 and LYP steel reaches a horizontal state upon fracture of their angles.

Fig. 22 shows the increase in total energy dissipation of the connection using LYP steel. It can be seen that employing LYP steel in the angles increases the total energy dissipation in all of the specimens. Significant increase in total energy dissipation of specimen 20s-18 is due to the reason that this specimen was designed to experience angle fracture and hence it undergoes more plastic deformation. Also as mentioned earlier this specimen is subjected to more loading cycles.

The results shows that using LYP in energy dissipater devices of a PTED connection considerably improve the seismic performance of the structure. In a severe earthquake, LYP steel can dissipate significant amount of input energy and therefore minimize the damage to the structural elements. It can also tolerate more loadig cycles without undergoing fracture which helps prevent the collapse of the structure.

5. Conclusion

This paper intends to provide a detailed FE modeling procedure for simulating the failure modes of PTED connections. For this purpose, non-linear finite element models of three PTED connection specimens were developed and analyzed under cyclic loading. These specimens experienced failure modes of beam local buckling, strand yielding and angle fracture in the experiment. Explicit analysis method was used to eliminate the convergence problem due to extensive yielding and fracture in the models. The lateral load-displacement responses and failure modes of models were validated against available experimental results. Since one of the applications of modeling failure is to be able to find solutions for preventing the damage or enhancing the behavior of the systems, a method was investigated to resolve the fracture in the angles which included replacing the A572 steel in angles with LYP steel. The hysteresis behavior of the models with LYP steel angles was studied in terms of force-displacement response, total energy dissipation capacity, plastic dissipation and fracture initiation point. Based on the results of this paper, following conclusions were drawn:

- (1) The analytical results were in good agreement with experimental data. Like the experiment, the FE model of specimen 36s-20-P did not experience any failure mode or significant damage. Only the beam web was subjected to buckling that at 4% drift had a single wave with amplitude of 9 mm which has negligible difference with the amount reported in the experiment.
- (2) The FE model of specimen 16s-45 underwent the failure mode of strand yielding. The exact three strands as in the experiment

reach their ultimate load in the FE model in drifts which were approximately similar to the experiment. The lateral load-displacement curve of the FE model showed more strength degradation than that of the experiment which was due to modeling the strands a single integrated element instead of several wires in a protection layer.

- (3) The FE model of specimen 20s-18 experienced failure mode of angles fracture and similar to the experiment all four top-and-seat angles fractured at the drift of 4%. The results illustrate that the employed methods for modeling failure modes in this study, which are mostly used in small scale, can be adopted for simulating the behavior of full scale complex models and achieve results with adequate accuracy.
- (4) Energy dissipation in models with LYP steel angles is considerably greater than those with A572 steel. Using LYP steel defers the fracture point from 4% to 7% drift and increased the total energy dissipation by 38%, 44% and 222% in specimen 36s-20-P, 16s-45 and 20s-18, respectively. Also using LYP steel in angles significantly improves the seismic performance of the PTED frame. Since it can undergo more loading cycles, therefore in a severe earthquake condition using LYP helps prevent or postpone the collapse of the structure.

References

- [1] D.K. Miller, Lessons learned from the Northridge earthquake, *Eng. Struct.* 20 (4–6) (1998) 249–260.
- [2] R. Tremblay, A. Filiatrault, Seismic performance of steel moment resisting frames retrofitted with a locally reduced beam section connection, *Can. J. Civ. Eng.* 24 (1) (1997) 78–89.
- [3] M.D. Engelhardt, T.A. Sabol, Reinforcing of steel moment connections with cover plates: benefits and limitations, *Eng. Struct.* 20 (4–6) (1998) 510–520.
- [4] C.-M. Uang, Q.-S.K. Yu, S. Noel, J. Gross, Cyclic testing of steel moment connections rehabilitated with RBS or welded haunch, *J. Struct. Eng.* 126 (1) (2000) 57–68.
- [5] M. Shiravand, A. Deylami, Technical papers: application of full depth side plate to moment connection of I-beam to double-I column, *Adv. Struct. Eng.* 13 (6) (2010) 1047–1062.
- [6] M.M. Garlock, J.M. Ricles, R. Sause, Experimental studies of full-scale posttensioned steel connections, *J. Struct. Eng.* 131 (3) (2005) 438–448.
- [7] J. Ricles, R. Sause, S. Peng, L. Lu, Experimental evaluation of earthquake resistant posttensioned steel connections, *J. Struct. Eng.* 128 (7) (2002) 850–859.
- [8] J.M. Ricles, R. Sause, M.M. Garlock, C. Zhao, Posttensioned seismic-resistant connections for steel frames, *J. Struct. Eng.* 127 (2) (2001) 113–121.
- [9] M.M. Garlock, J.M. Ricles, R. Sause, Cyclic load tests and analysis of bolted top-and-seat angle connections, *J. Struct. Eng.* 129 (12) (2003) 1615–1625.
- [10] C. Christopoulos, A. Filiatrault, C.-M. Uang, B. Folz, Posttensioned energy dissipating connections for moment-resisting steel frames, *J. Struct. Eng.* 128 (9) (2002) 1111–1120.
- [11] C.C. Chou, J.H. Chen, Y.C. Chen, K.C. Tsai, Evaluating performance of post-tensioned steel connections with strands and reduced flange plates, *Earthquake Eng. Struct. Dynam.* 35 (9) (2006) 1167–1185.
- [12] G. Vasdravellis, T.L. Karavasilis, B. Uy, Large-scale experimental validation of steel posttensioned connections with web hourglass pins, *J. Struct. Eng.* 139 (6) (2012) 1033–1042.
- [13] C.-C. Chou, Y.-J. Lai, Post-tensioned self-centering moment connections with beam bottom flange energy dissipators, *J. Constr. Steel Res.* 65 (10–11) (2009) 1931–1941.
- [14] G. Vasdravellis, T.L. Karavasilis, B. Uy, Finite element models and cyclic behavior of self-centering steel post-tensioned connections with web hourglass pins, *Eng. Struct.* 52 (2013) 1–16.
- [15] S. Moradi, M.S. Alam, Finite-element simulation of posttensioned steel connections with bolted angles under cyclic loading, *J. Struct. Eng.* 142 (1) (2015) 04015075.
- [16] H. Hibbit, B. Karlsson, E. Sorensen, ABAQUS User Manual, Version 6, Vol. 12 Simulia, Providence, RI, 2012.
- [17] M.E.M. Garlock, Design, Analysis, and Experimental Behavior of Seismic Resistant Post-tensioned Steel Moment Resisting Frames, (2002).
- [18] F. Liao, W. Wang, Y. Chen, Ductile fracture prediction for welded steel connections under monotonic loading based on micromechanical fracture criteria, *Eng. Struct.* 94 (2015) 16–28.
- [19] H. Amiri, A. Aghakouchak, S. Shahbeyk, M. Engelhardt, Finite element simulation of ultra low cycle fatigue cracking in steel structures, *J. Constr. Steel Res.* 89 (2013) 175–184.
- [20] J. Fernandez-Ceniceros, A. Sanz-Garcia, F. Antoñanzas-Torres, F. Martinez-de-Pison, A numerical-informational approach for characterising the ductile behaviour of the T-stub component. Part I: Refined finite element model and test validation, *Eng. Struct.* 82 (2015) 236–248.
- [21] W. Wang, C. Fang, X. Qin, Y. Chen, L. Li, Performance of practical beam-to-SHS column connections against progressive collapse, *Eng. Struct.* 106 (2016) 332–347.
- [22] M.A. Bradford, X. Liu, Flexural-torsional buckling of high-strength steel beams, *J. Constr. Steel Res.* 124 (2016) 122–131.
- [23] C. Couto, P.V. Real, N. Lopes, B. Zhao, Local buckling in laterally restrained steel beam-columns in case of fire, *J. Constr. Steel Res.* 122 (2016) 543–556.
- [24] A.C. Lam, M.C. Yam, C. Fang, Strength and behaviour of reinforced double-coped beams against local web buckling, *J. Constr. Steel Res.* 138 (2017) 38–50.
- [25] A.C. Lam, Y. Zhang, Y. Qin, M.C. Yam, V. Iu, Design for inelastic local web buckling of coped beams, *J. Constr. Steel Res.* 125 (2016) 173–189.
- [26] M.L. Morrison, T. Hassan, Resilient welded steel moment connections by enhanced beam buckling resistance, *J. Constr. Steel Res.* 127 (2016) 77–91.
- [27] A.T. Myers, Testing and Probabilistic Simulation of Ductile Fracture Initiation in Structural Steel Components and Weldments, Stanford University, 2009.
- [28] S. Kmet, E. Stanova, G. Fedorko, M. Fabian, J. Brodniansky, Experimental investigation and finite element analysis of a four-layered spiral strand bent over a curved support, *Eng. Struct.* 57 (2013) 475–483.
- [29] E. Stanova, G. Fedorko, M. Fabian, S. Kmet, Computer modelling of wire strands and ropes part II: Finite element-based applications, *Adv. Eng. Softw.* 42 (6) (2011) 322–331.
- [30] E. Stanova, G. Fedorko, S. Kmet, V. Molnar, M. Fabian, Finite element analysis of spiral strands with different shapes subjected to axial loads, *Adv. Eng. Softw.* 83 (2015) 45–58.
- [31] R. Judge, Z. Yang, S. Jones, G. Beattie, Full 3D finite element modelling of spiral strand cables, *Constr. Build. Mater.* 35 (2012) 452–459.
- [32] F.A. McClintock, A Criterion for Ductile Fracture by the Growth of Holes, ASME, 1968.
- [33] J.R. Rice, D.M. Tracey, On the ductile enlargement of voids in triaxial stress fields*, *J. Mech. Phys. Solids* 17 (3) (1969) 201–217.
- [34] G.R. Johnson, W.H. Cook, Fracture characteristics of three metals subjected to various strains, strain rates, temperatures and pressures, *Eng. Fract. Mech.* 21 (1) (1985) 31–48.
- [35] Z. Zhou, L. Jia, Damage index for crack initiation of structural steel under cyclic loading, *J. Constr. Steel Res.* 114 (2015) 1–7.
- [36] H. Kuwamura, Transition between fatigue and ductile fracture in steel, *J. Struct. Eng.* 123 (7) (1997) 864–870.
- [37] T.L. Panontin, S.D. Sheppard, The Relationship Between Constraint and Ductile Fracture Initiation as Defined by Micromechanical Analyses, *Fracture Mechanics: 26th Volume, ASTM International, West Conshohocken, 1995*, pp. 54–85.
- [38] A. Kanvinde, G. Deierlein, Finite-element simulation of ductile fracture in reduced section pull-plates using micromechanics-based fracture models, *J. Struct. Eng.* 133 (5) (2007) 656–664.
- [39] M.A. Miner, Cumulative damage in fatigue, *J. Appl. Mech.* 12 (3) (1945) A159–A164.
- [40] L.-J. Jia, H. Kuwamura, Ductile fracture model for structural steel under cyclic large strain loading, *J. Constr. Steel Res.* 106 (2015) 110–121.
- [41] H. Hooputra, H. Gese, H. Dell, H. Werner, A comprehensive failure model for crashworthiness simulation of aluminium extrusions, *Int. J. Crashworth.* 9 (5)

- (2004) 449–464.
- [42] Y. Bao, T. Wierzbicki, On fracture locus in the equivalent strain and stress triaxiality space, *Int. J. Mech. Sci.* 46 (1) (2004) 81–98.
 - [43] Y.-W. Lee, T. Wierzbicki, Quick fracture calibration for industrial use, Massachusetts Institute of Technology, Impact & Crashworthiness Laboratory Report (115), 2004.
 - [44] H. Yu, D. Jeong, Application of a stress triaxiality dependent fracture criterion in the finite element analysis of unnotched Charpy specimens, *Theor. Appl. Fract. Mech.* 54 (1) (2010) 54–62.
 - [45] H. Yu, D.Y. Jeong, Impact dynamics and puncture failure of pressurized tank cars with fluid–structure interaction: A multiphase modeling approach, *Int. J. Impact Eng.* 90 (2016) 12–25.
 - [46] Y. Bao, T. Wierzbicki, On the cut-off value of negative triaxiality for fracture, *Eng. Fract. Mech.* 72 (7) (2005) 1049–1069.
 - [47] S. Novak, A Fracture Mechanics Study on Resistance of ASTM A36, A572, and A517 Grade F Structural Steels to Stress-Corrosion Crack Growth in Salt Water2, *Fracture Mechanics: Fourteenth Symposium-STP 791*, ASTM International, 1983, p. 415.
 - [48] E. Saeki, M. Sugisawa, T. Yamaguchi, A. Wada, Mechanical properties of low yield point steels, *J. Mater. Civ. Eng.* 10 (3) (1998) 143–152.
 - [49] A. AISC, AISC 341-05, Seismic provisions for structural steel buildings, Chicago (IL), American Institute of Steel Construction, 2005.
 - [50] S.J. Venture, Protocol for Fabrication, Inspection, Testing, and Documentation of Beam-column Connection Tests and Other Experimental Specimens, Rep. No. SAC/BD-97, (1997), p. 2.
 - [51] J. Wang, Y. Shi, Y. Wang, Constitutive model of low-yield point steel and its application in numerical simulation of buckling-restrained braces, *J. Mater. Civ. Eng.* (2015) (04015142).
 - [52] G. De Matteis, R. Landolfo, F. Mazzolani, Seismic response of MR steel frames with low-yield steel shear panels, *Eng. Struct.* 25 (2) (2003) 155–168.
 - [53] S. Ming-hsiang, S. Wen-pei, G. Cheer-germ, Investigation of newly developed added damping and stiffness device with low yield strength steel, *J. Zhejiang Univ. (Sci.)* 5 (3) (2004) 326–334.
 - [54] M. Nakashima, Strain-hardening behavior of shear panels made of low-yield steel. I: test, *J. Struct. Eng.* 121 (12) (1995) 1742–1749.
 - [55] S.-J. Chen, C. Jhang, Seismic Behavior of Low Yield Point Steel Plate Shear Wall, *Structures Congress 2008*, Vancouver, British Columbia, Canada, (2008), pp. 1–10.
 - [56] S.-J. Chen, C. Jhang, Experimental study of low-yield-point steel plate shear wall under in-plane load, *J. Constr. Steel Res.* 67 (6) (2011) 977–985.
 - [57] T. Suzuki, Seismic control devices using low-yield-point steel, *Nippon Steel Tech. Rep.* 77 (7) (1998) 65–72.
 - [58] M.M. Garlock, R. Sause, J.M. Ricles, Behavior and design of posttensioned steel frame systems, *J. Struct. Eng.* 133 (3) (2007) 389–399.